IOP Publishing Measurement Science and Technology
Meas. Sci. Technol. 31 (2020) 055402 (10pp) https://doi.org/10.1088/1361-6501/ab6278

Ridge extraction based on adaptive variable-bandwidth cost functions by edge detection of time frequency images

Chunhong Dou[1] **and Jinshan Lin**[2]

[1] School of Information and Control Engineering, Weifang University, No. 5147 Dong Feng Dong Street, Weifang 261061, People's Republic of China
[2] School of Mechatronics and Vehicle Engineering, Weifang University, No. 5147 Dong Feng Dong Street, Weifang 261061, People's Republic of China

E-mail: jslinmec@hotmail.com and jslinmec@wfu.edu.cn

Received 13 October 2019, revised 15 November 2019
Accepted for publication 16 December 2019
Published 31 January 2020

Abstract

Ridge extraction of a time frequency image (TFI) can serve to estimate an instantaneous frequency of a signal. However, there is a considerable difficulty in ridge extraction of a multi-ridge TFI due to mutual interference between ridges. Some traditional methods for ridge extraction fail to resolve this difficulty. The one-step cost function (OSCF), a typical method for processing a multi-ridge TFI, lacks self-adaptation in determining searching regions of a targeted ridge. To overcome this question, this paper proposes an adaptive variable-bandwidth cost function (AVBCF) for ridge extraction. Firstly, a TFI is acquired by time frequency analysis of a signal. Afterwards, the TFI is filtered into a binary image by a Canny detector. Also, some dispersive ridges in the binary image serve to form a synthetic dispersive ridge. Next, searching regions of a targeted ridge are estimated by projecting statistics of edges of the synthetic dispersive ridge to the targeted ridge. Next, the AVBCF is compared with the OSCF and some widespread methods numerally and experimentally. The results demonstrate that the AVBCF performs better than the other methods.

Keywords: ridge extraction, edge detection, adaptive variable-bandwidth cost function, time frequency image, planetary gearbox

(Some figures may appear in colour only in the online journal)

1. Introduction

Machines usually bear variable loads and maintain an unsteady speed [1]. Therefore, vibrations of machines generally feature nonstationarity and nonlinearity. In this case, it is a challenging task to estimate an instantaneous frequency (IF) of a mechanical part in unsteady conditions [2]. Typically, the kinematics of a mechanical part presents itself as a ridge in a time frequency image (TFI) converted from a vibration signal from a machine. Here, a ridge refers to a curve formed by the most energy-intensive points in a TFI [3–5]. For this reason, reflecting a change of frequencies with time, a ridge can discover instantaneous properties of a mechanical part [1, 3–6]. Consequently, ridge extraction from a TFI of a signal can serve to recover an IF of a mechanical part [7–9]. Nonetheless, a complex signal from a machine in unsteady conditions usually contains a number of components, which theoretically correspond to the same number of ridges in a TFI of this signal. As a consequence, mutual interference between these ridges considerably increases difficulties in recovering an IF of a mechanical part from a signal [10].

In past decades, several algorithms for ridge extraction have been designed [3–5, 11–14]. As the simplest one among them, the modulus maximum method (MMM) directly detects the most energy-intensive point along frequencies of a TFI at each instant [11]. When applied to extract a targeted ridge from a multi-ridge TFI, the MMM may pick up points from a ridge different from the targeted ridge. Consequently, a targeted ridge

extracted by the MMM often lacks continuity. Accordingly, the MMM is not applicable to a complex signal containing many components [4]. For addressing this problem, the one-step cost function (OSCF) was proposed [10, 15]. The OSCF limits researching regions of a targeted ridge within a range of constant bandwidth and centers a searching region of some point on the previous neighbor of this point on a targeted ridge. Accordingly, compared with the MMM, the OSCF considers both continuity and accuracy of a ridge. However, the OSCF seemingly lacks self-adaptation in determining searching regions of a targeted ridge due to invariance of researching bandwidth and dependence on inertia of locations of two consecutive points on the targeted ridge. As a result, a searching region of a point on a targeted ridge, provided by the OSCF, either may exclude the point from the searching region or may introduce excessive noise. Also, a dual path optimization method for ridge estimation, proposed in [2], seemingly suffers from the same deficiency as the OSCF. Consequently, the OSCF still leaves some to be desired.

On many occasions, a vibration signal is preprocessed by time-frequency analysis (TFA) methods. Currently, TFA methods mainly include short-time Fourier transform (STFT), Wigner–Ville distribution, wavelet transform (WT), empirical mode decomposition and variational mode decomposition. These TFA methods all have own advantages and disadvantages, and can find their appropriate use in different cases. As two popular methods, STFT and WT have been widely employed in vibration signal analysis. This paper uses STFT and WT to preprocess vibration signals. In doing so, a vibration signal can be transformed into a TFI by TFA methods. Because a real signal usually contains many components, a TFI transformed from the real signal consists of multiple ridges, each of which refers to kinematics of a mechanical part. Since a ridge locally represents the most energy-intensive points in a TFI, there may be an energy gradient around the ridge in the TFI. As a result, dispersion of a ridge may appear. In doing so, a dispersive ridge can be outlined by its edges. In this manner, statistics of a ridge enclosed in its edges can be estimated by analyzing distribution of these edges. Along this path, projections of these statistics pave a possible way for determining areas covering the targeted ridge. As a consequence, this paper proposes an adaptive variable-bandwidth cost function (AVBCF). Thus, the AVBCF searches a point in a variable-bandwidth region independent of the previous neighbor of this point on a targeted ridge. The process of performing the AVBCF is stated as follows. Firstly, a vibration signal is mapped to a TFI using STFT. Secondly, a TFI zone, which contains some dispersive ridges and has a relatively high signal-to-noise ratio (SNR), is filtered into a binary image by the Canny detector. In this way, these dispersive ridges can be outlined by their edges in the binary image. Thirdly, the Grubbs test is applied to exclude outliers, which represent noise, from edges of each dispersive ridge. Fourthly, these dispersive ridges are proportionally superimposed on one of them for forming a synthetic dispersive ridge with clear and complete edges. Again, the Grubbs test is applied to exclude outliers from edges of the synthetic dispersive ridge. Next, a central line of the synthetic dispersive ridge and the confidence interval of the central line at 95% confidence level are projected to the targeted ridge according to kinematic relations between the targeted ridge and the synthetic dispersive ridge. In the following, the AVBCF is used for extracting the targeted ridge. Subsequently, the performance of the AVBCF is benchmarked against the OSCF numerically. Also, the performance of the AVBCF is compared with the OSCF and some widespread methods using a signal from a variable-speed planetary gearbox. The results indicate that the AVBCF delivers a better performance over the others.

The remaining contents of this paper are structured as follows. Section 2 provides an introduction to the OSCF. Section 3 proposes the AVBCF. Section 4 evaluates the performance of the AVBCF numerically and experimentally, and opens up a discussion. Section 5 concludes this paper.

2. OSCF

The OSCF is reported as follows [10].

(1) Convert a signal into a TFI using STFT;
(2) Define a local cost function CF_k at the kth instant as

$$CF_k = |f_k(i) - f_{k-1}(c)|^2 - e_k|TF(t_k, f_k(i))|^2, \quad k = 2, 3, \ldots, m \tag{1}$$

where

t_k The kth instant
f_k The frequency for the most energy-intensive point at t_k
$TF(t,f)$ Energy representations of the analyzed signal at instant t and frequency f
m The number of instants in the TFI
n The number of frequencies in the TFI
$f_k(c)$ The frequency for the most energy-intensive point determined by minimizing CF_k at t_k
$f_k(i)$ A potential candidate for $f_k(c)$, $i = 1, 2, \ldots n$
e_k The weighted factor

As seen in equation (1), for making CF_k minimal, the former term should be as small as possible and the latter one as large as possible. Thus, the former term aims to maintain continuity of a ridge and the latter to identify an energy peak in a range of frequencies at t_k. In this respect, the OSCF considers both continuity and accuracy of a ridge when applied to ridge extraction.

For eliminating mutual interference between ridges, the OSCF limits searching regions of a targeted ridge within a range of constant bandwidth. The OSCF defines a local searching region FB_k at t_k below:

$$FB_k = [f_{k-1}(c) - f_w, f_{k-1}(c) + f_w], \quad k = 2, 3, \ldots, m \tag{2}$$

$$e_k = \left[\frac{f_w}{\max\limits_{f_k \in FB_k} [TF(t_k, f_k)]}\right]^2, \quad k = 2, 3, \ldots, m. \tag{3}$$

Here, f_w is a half-width of FB_k, remaining constant once set. As seen in equation (2), FB_k is centered on $f_{k-1}(c)$. To clarify this issue, figure 1 exemplifies how the OSCF determines a

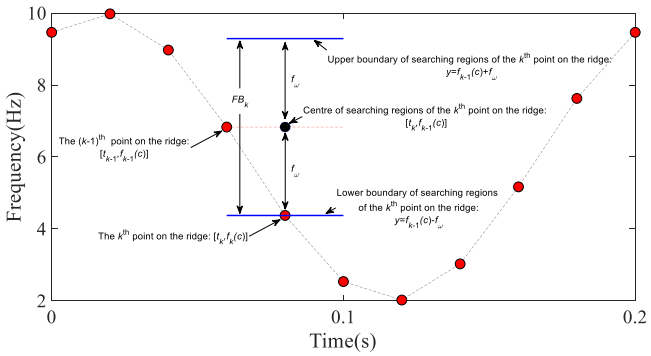

Figure 1. A local searching region of a point on a targeted ridge in the OSCF.

searching region of a point on a targeted ridge using equation (2). As described in figure 1, FB_k can cover an energy peak at t_k if and only if $f_w > |f_k(c) - f_{k-1}(c)|$. However, exceeding largeness of f_w possibly makes FB_k cover a part of a different ridge. Accordingly, the OSCF seemingly leaves much to be desired in exactly determining searching regions of a targeted ridge.

3. AVBCF

This paper proposes the AVBCF for overcoming the deficiency of the OSCF. The AVBCF defines a cost function CF_k as

$$CF_k = |f_k(i) - f_k(pmc)|^2 - e_k|TF(t_k, f_k(i))|^2 \quad k = 1, 2, \ldots, m \tag{4}$$

and does a local searching region FB_k at t_k as

$$FB_k = \left[f_k(pmc) - f_w^k, f_k(pmc) + f_w^k\right] \quad k = 1, 2, \ldots, m \tag{5}$$

$$e_k = \left[\frac{f_w^k}{\max\limits_{f_k \in FB_k} [TF(t_k, f_k)]}\right]^2, \quad k = 1, 2, \ldots, m. \tag{6}$$

Here, $f_k(pmc)$ denotes a value on the central line projected at t_k and f_w^k indicates a half of the confidence interval projected at t_k.

Afterwards, the AVBCF is applied to ridge extraction. Firstly, some dispersive ridges are outlined by their edges by the Canny detector [16, 17]. Then, these dispersive ridges serve to synthesize a dispersive ridge with clear and complete edges. Here, the Grubbs test is employed to exclude outliers from edges of raw dispersive ridges and of the synthetic one. Next, the central line of the synthetic dispersive ridge and the confidence interval of the central line are projected to the targeted ridge. Moreover, projections of the central line and of the confidence interval serve as a reference and searching regions of the targeted ridge, respectively. Also, introduction to the Grubbs test and to the confidence interval of a dispersive ridge is given in appendices A and B, respectively. The AVBCF is stated as follows.

Step 1: Generate a TFI using STFT.
Step 2: Filter a TFI zone with a relatively high SNR into a binary image by the Canny detector and outline some dispersive ridges by their edges.
Step 3: Use the Grubbs test to exclude outliers from edges of each dispersive ridge.
Step 4: Proportionally superimpose these dispersive ridges on one of them for synthesizing a dispersive ridge with clear and complete edges.
Step 5: Use the Grubbs test to exclude outliers from edges of the synthetic ridge.
Step 6: Calculate the central line of the synthetic ridge, smooth the central line in a span of five points using a moving average filter and estimate the confidence interval of the central line at 95% confidence level.
Step 7: Project the central line and the confidence interval thereof to a targeted ridge according to kinematic relations between the targeted ridge and the synthetic ridge.
Step 8: Define projections of the central line and the confidence interval as the reference and the search regions of the targeted ridge, respectively.
Step 9: Extract the targeted ridge using the AVBCF.

In this place, it is very important for the Canny detector to appropriately set a double threshold [16, 17]. A too high threshold may lead to loss of important information, while a too low one may does inclusion of irrelevant information. Nevertheless, a double threshold applicable everywhere scarcely exists. Fortunately, [17] has designed an empirical scheme for determining a high threshold: firstly, an image is filtered by a Wiener filter; then, a global histogram of the filter responses is taken; next, the position of the low percentile not more than 80% is recommended for determining the high threshold. In this paper, the high threshold is taken at the 70% percentile and a low threshold is empirically set as 0.4 time the high threshold. A more detailed introduction to the Canny detector is provided in [17].

Furthermore, some rules should be followed for choosing the TFI zone in Step 2. Firstly, the chosen TFI zone should contain at least two dispersive ridges for synthesis. Secondly, dispersive ridges in the chosen TFI zone should provide a marked contrast to backgrounds for convenience of edge detection. Thirdly, dispersive ridges in the chosen TFI zone can be clearly separated from each other for excluding outliers from each of these ridges.

4. Performance verification of the AVBCF

4.1. Numerical verification

In this subsection, a simulative signal modeling vibrations of a planetary gearbox was constructed for evaluating the feasibility of the AVBCF. Here, the simulative signal contains three components, mixed with weak low-frequency and strong high-frequency noise. Additionally, there is a proportional relation between IFs of these three components. The

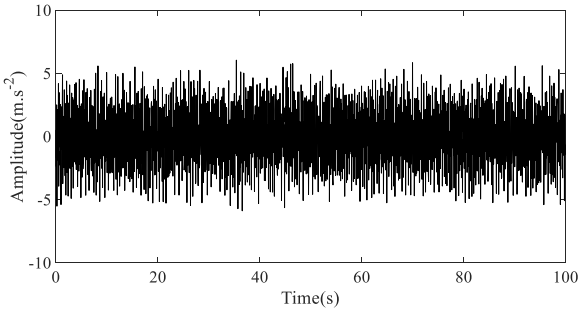

Figure 2. A simulative signal modeling vibrations of a planetary gearbox.

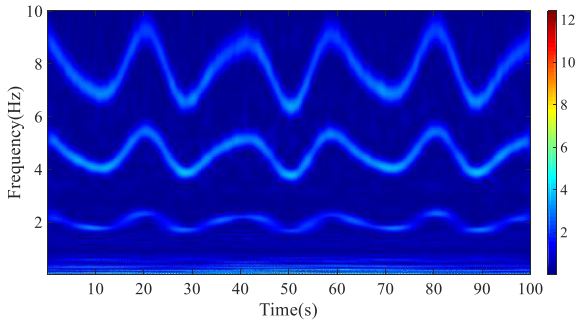

Figure 3. The WT TFI of the simulative signal.

simulative signal x with a size of $N = 2000$ and a sampling frequency of $f_s = 20\,\text{Hz}$ is expressed as follows:

$$x = x_0 + noiseOne + noiseTwo \tag{7}$$

$$\begin{aligned}
x_0 &= x_1 + x_2 + x_3,\\
x_1 &= \left[1 + \tfrac{1}{3}\cos\left(\tfrac{2\pi t}{9}\right)\right]\cos\left[\begin{array}{c} 4\pi t + 6\sin\left(\tfrac{\pi t}{10}\right) + \\ \cos\left(\tfrac{\pi t}{6}\right)\end{array}\right],\\
t &= (0, 1, \ldots N-1)/f_s,\\
x_2 &= 2\cos\left[2.3\left(4\pi t + 6\sin\left(\tfrac{\pi t}{10}\right) + \cos\left(\tfrac{\pi t}{6}\right)\right)\right],\\
t &= (0, 1, \cdots N-1)/f_s,\\
x_3 &= 2.5\cos\left[3.9\left(4\pi t + 6\sin\left(\tfrac{\pi t}{10}\right) + \cos\left(\tfrac{\pi t}{6}\right)\right)\right],\\
t &= (0, 1, \ldots N-1)/f_s,\\
noiseOne &= 0.1 \cdot std\,(x_0) \cdot lowfrequencyNoise,\\
noiseTwo &= 0.2 \cdot std\,(x_0) \cdot highfrequencyNoise.
\end{aligned} \tag{8}$$

Here, the signs *lowfrequencyNoise* and *highfrequencyNoise* represent the low-frequency noise in a frequency range of 0–3 Hz and the high-frequency noise in a frequency range of 3–10 Hz, respectively; the sign std $(\cdot)$ means to calculate the standard deviation. The simulative signal is depicted in figure 2.

The objective of the simulation is to recover the IF of the component x_3 from the simulative signal. To begin with, figure 3 illustrates the use of WT in examining the simulative signal. Here, the WT TFI was evaluated at 256 frequencies and 2000 instants using a complex Morlet wavelet with a bandwidth parameter of 3 and a center frequency of 4. Next, the STFT was employed to analyze the simulative signal and the results are displayed in figure 4. Here, the STFT TFI was evaluated at 257 frequencies and 485 instants using a Hamming window of length 64, with an overlapping window of length 60. As displayed in figures 3 and 4, some dispersive

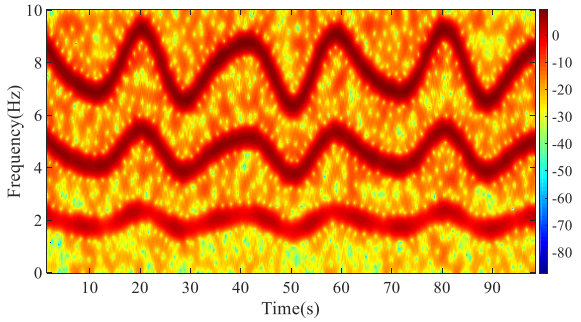

Figure 4. The STFT TFI of the simulative signal.

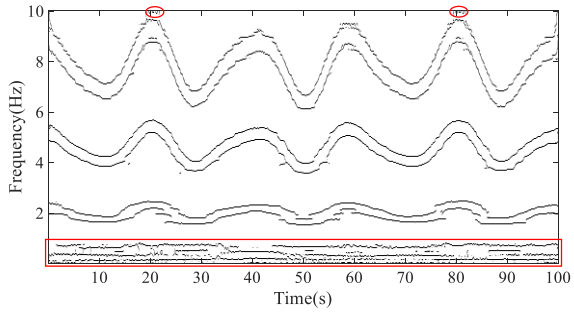

Figure 5. Edges detected from the WT TFI of the simulative signal using the Canny detector, where some blurred areas are marked in red.

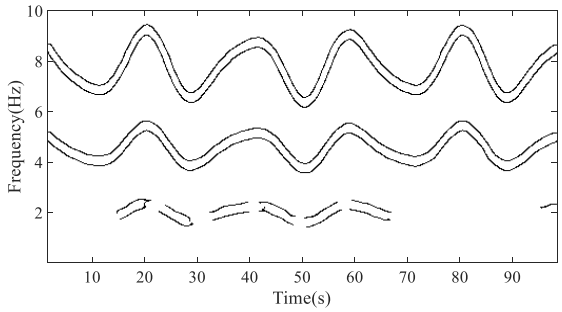

Figure 6. Edges detected from the STFT TFI of the simulative signal using the Canny detector.

ridges indeed emerge. Additionally, there exists a proportional relation between frequencies relative to these dispersive ridges, which displays kinetics contained in the simulative signal. Afterwards, figures 5 and 6 display edges detected by the Canny detector from the WT TFI and from the STFT TFI, respectively. Consequently, a comparison between figures 5 and 6 shows that the edges detected from the STFT TFI is clearer than those from the WT TFI. Since clear and complete, edges of the upper dispersive ridge in figure 6 can serve directly as searching regions of a targeted ridge. In the following, the targeted ridge was extracted using the AVBCF. Subsequently, figures 7(a) and (b) draws a comparison between the estimated IF using the AVBCF and the theoretical value and reports relative errors between them, respectively. Moreover, the OSCF was employed to recover the IF of the component x_3 from the simulative signal. Here, a half-bandwidth f_w of searching regions for the targeted ridge was assigned to 0.7 Hz in the OSCF. Figures 8(a) and (b) compares the estimated IF using the OSCF with the theoretical value and reports relative errors

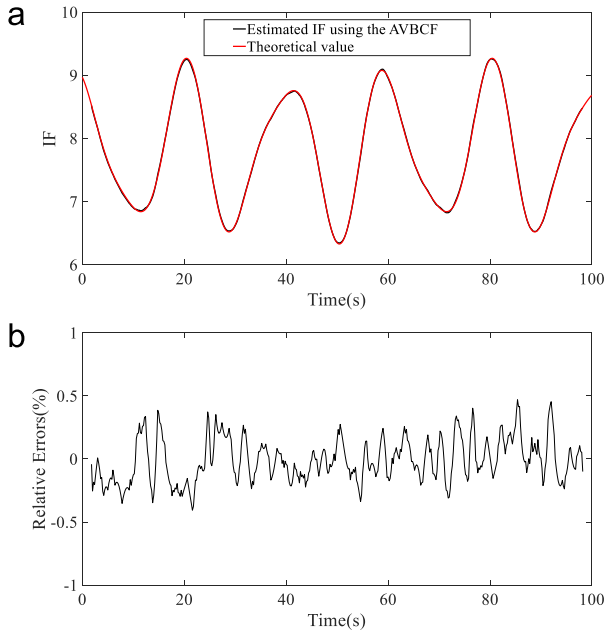

Figure 7. (a) Comparisons between the estimated IF using the AVBCF and the theoretical value in the simulation, (b) relative errors between the estimated IF using the AVBCF and the theoretical value.

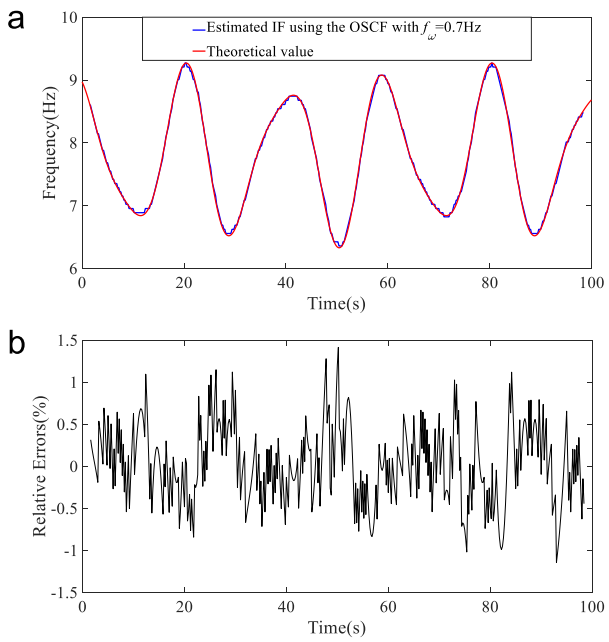

Figure 8. (a) Comparisons between the estimated IF using the OSCF and the theoretical value in the simulation, (b) relative errors between the estimated IF using the OSCF and the theoretical value.

between them, respectively. As a consequence, a comparison between figures 7(b) and 8(b) indicates that the AVBCF outperforms the OSCF in the simulation.

4.2. Experimental verification

The Fourth International Conference on Condition Monitoring of Machinery in Non-stationary Operations (CMMNO2014) sponsored a contest for assessing the performance of

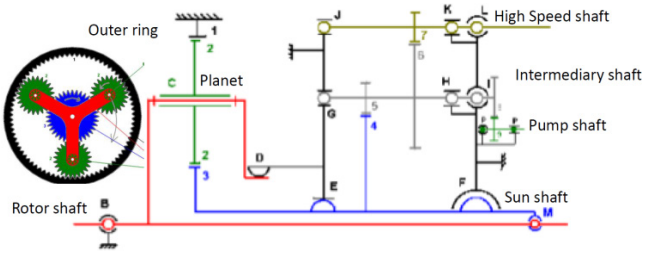

Figure 9. A kinematic sketch of the planetary gearbox.

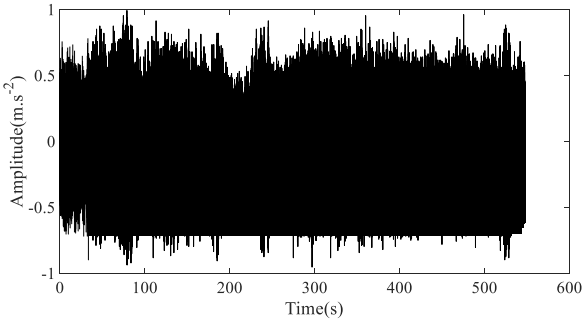

Figure 10. A signal collected from the planetary gearbox, provided in CMMNO 2014.

Table 1. Kinematic parameters of the planetary gearbox.

Gear labels	Teeth
1	123
2 (3 planets)	50
3	21
4	93
5	22
6	120
7	29
8	63
9	23
10	10
11	13

monitoring and diagnostic algorithms in non-stationary operations [18–20]. The contest provided a vibration signal collected from a wind turbine planetary gearbox, whose kinematic sketch is presented in figure 9. The signal was recorded with IFM-Electronics VSE002 acquisition systems by an accelerometer fixed on the gearbox housing close to the epicyclic gear train, with a size of 2736 825 points and a sampling frequency of 5000 Hz. The signal provided in the contest is depicted in figure 10. During recording the signal, a speed of the input shaft fluctuates between 13 and 15 revolutions per minute (RPM). Evidently, a range of 13 RPM–15 RPM matches 0.22 Hz–0.25 Hz. Kinematic parameters and details of the planetary gearbox are provided in tables 1 and 2, respectively. One objective of the contest is to recover the IF of the high speed shaft. To reach this objective, a ridge in a TFI of this gearbox vibration signal should be extracted.

To start with, WT was adopted to investigate the gearbox vibration signal and the results are displayed in figure 11. Here, the WT TFI was evaluated at 256 frequencies and 2736 825 instants using a complex Morlet wavelet with a

Table 2. Kinematic details of the planetary gearbox.

Kinematic elements	Order
Input shaft	1
Sun gear shaft	6.86
Intermediate shaft	28.99
Output shaft	119.95
Gear pairs ½	123
Gear pairs 2/3	123
Gear pairs 4/5	637.71
Gear pairs 6/7	3478.44

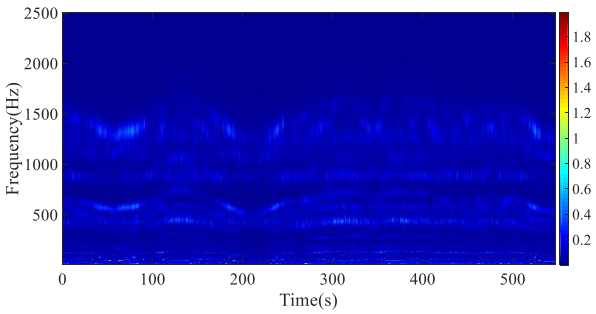

Figure 11. The WT TFI of the planetary gearbox signal.

bandwidth parameter of 3 and a center frequency of 3. In addition, the frequency resolution in the WT TFI cannot be set higher because of limitations of performances of the used computer, which remains identical in all the transformation. Afterwards, STFT was applied to explore the gearbox vibration signal and the results are displayed in figure 12(a). Here, the STFT TFI was evaluated at 19 201 frequencies and 5682 instants using a Hamming window of length 9600, with an overlapping window of length 9120. Since much clearer than the WT TFI in figure 11, the STFT TFI in figure 12(a) was examined for edge detection. Afterwards, the ridge centered on 280 Hz in figure 12(b) was chosen as the targeted ridge. Two reasons for this choice are provided as follows. Firstly, the targeted ridge is completely contained in the 200–320 Hz image zone, which is less disturbed by noise and other ridges. Secondly, the targeted ridge is the only potential candidate for the second harmonic of the meshing frequency of intermediate gear pairs 4/5.

In the following, a reference and searching regions of the targeted ridge were estimated by exploiting kinematic relations between different parts of the planetary gearbox. As exhibited in figure 12(a), there is an approximately proportional relation between these dispersive ridges, which exhibits local kinematics of the planetary gearbox. Moreover, with a relatively high SNR, the low-frequency image zone between 17 Hz and 93 Hz in figure 13 was investigated for estimating the reference and the searching regions of the targeted ridge. In addition, a close-up of the low-frequency image zone shows that the frequency relative to the lower dispersive ridge is nearly the meshing frequency of planet gear pairs 1/2. Also, as described in figure 13, the IFs for the middle dispersive ridge and for the upper dispersive ridge are almost two and three times that for the lower dispersive ridge, respectively. Then, the low-frequency image zone was filtered by

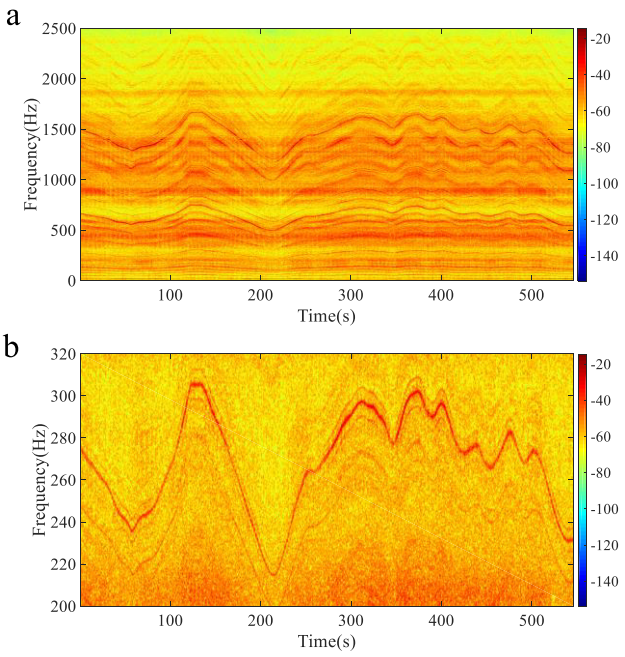

Figure 12. The STFT TFI of the planetary gearbox signal, (a) the whole image, (b) the 200–320 Hz zone.

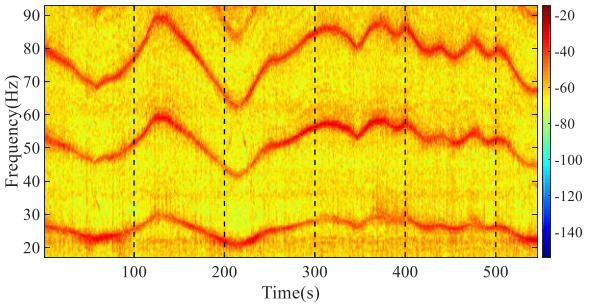

Figure 13. The STFT TFI zone chosen for edge detection, where artificial vertical dash lines in black assist in quantifying the relations between these three dispersive ridges.

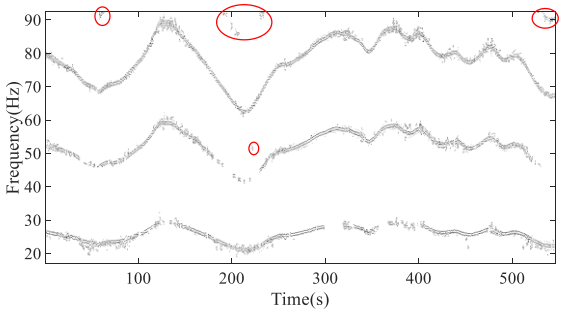

Figure 14. Edges detected from the image zone using the Canny detector, where some noisy areas are circled in red.

the Canny detector with two different thresholds 0.0063 and 0.0156 and the results are shown in figure 14. As shown in figure 14, in which some contaminated areas are circled in red, profiles of the upper dispersive ridge are mostly maintained but locally contaminated, while those of the middle and the lower dispersive ridges are less contaminated but leave several gaps. Subsequently, the Grubbs test was adopted to purify the binary image zone: firstly, separate the binary

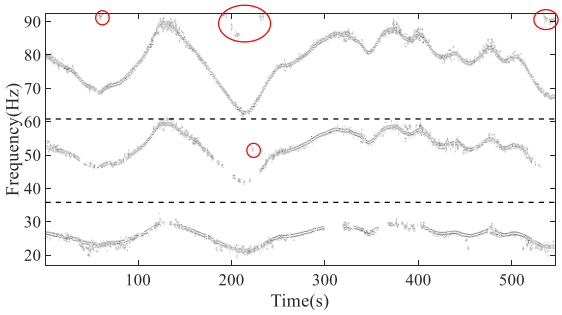

Figure 15. Separated dispersive ridges in the image zone, where artificial horizontal dash lines in black assist in distinguishing between different dispersive ridges and some noisy areas are circled in red.

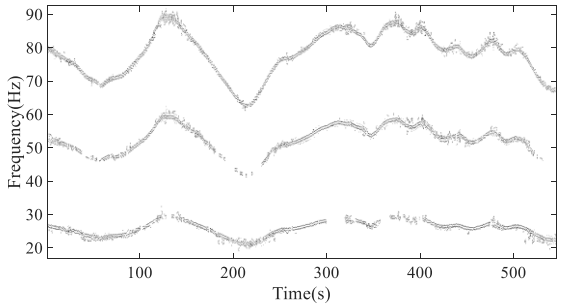

Figure 16. The refined dispersive ridges by the Grubbs test.

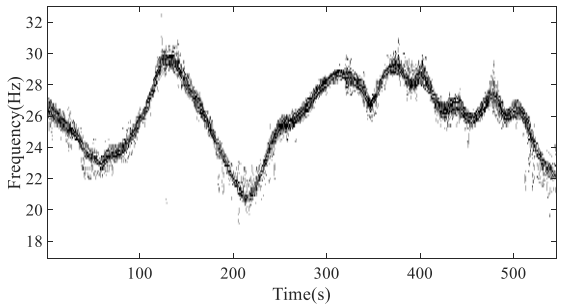

Figure 17. The synthetic dispersive ridge.

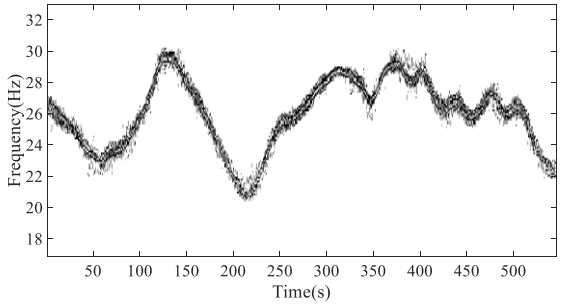

Figure 18. The refined synthetic dispersive ridge by the Grubbs test.

image zone in figure 14 into three non-overlapping regions, each of which contains only one dispersive ridge, as demonstrated in figure 15; then, apply the Grubbs test to exclude outliers from each of these raw dispersive ridges. Figure 16 exhibits the results purified by the Grubbs test. A comparison between figures 15 and 16 demonstrates that the outliers circled in red in figure 15 have been removed from figure 16.

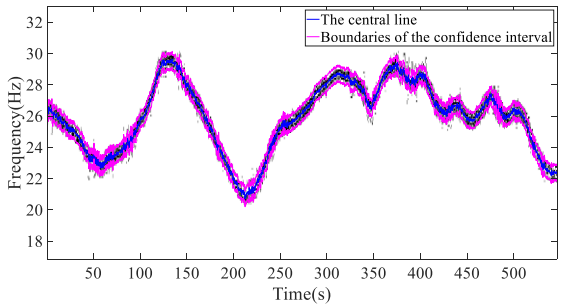

Figure 19. The central line of the synthetic dispersive ridge and the confidence interval of the central line at 95% confidence level.

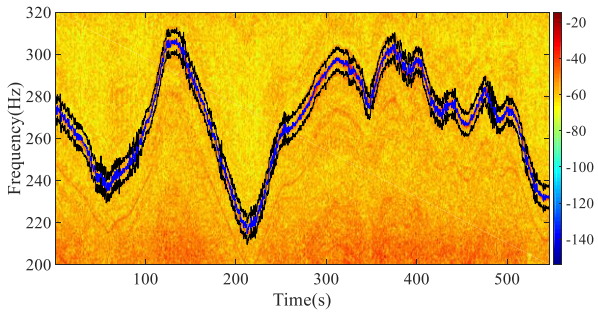

Figure 20. Projections of the central line and of the confidence interval at 95% confidence level to the targeted ridge, where the blue line stands for a reference of the targeted ridge and the black lines for boundaries of searching regions.

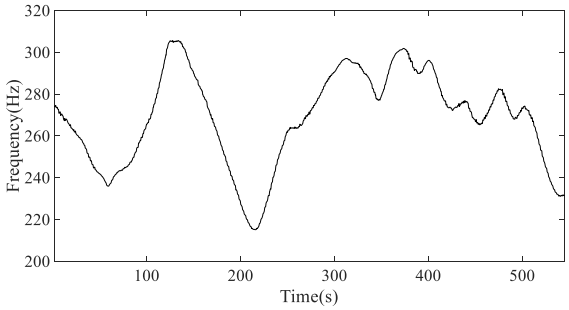

Figure 21. Extraction of the targeted ridge using the AVBCF.

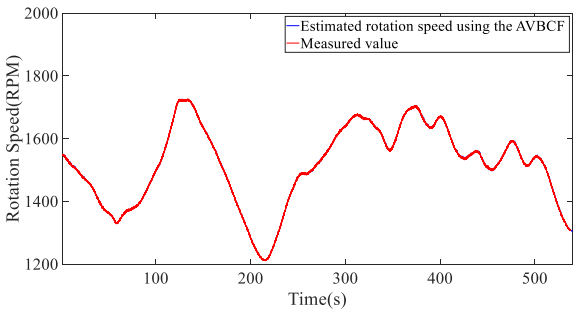

Figure 22. Comparisons between the estimated rotation speed using the AVBCF and the measured value.

Afterwards, the upper and the middle dispersive ridges were superposed proportionally on the lower one for constructing a synthetic one with clear and complete edges, as displayed in figure 17. Again, the Grubbs test was employed to further refine the synthetic dispersive ridge and the results are depicted in figure 18. A comparison between figures 17 and 18

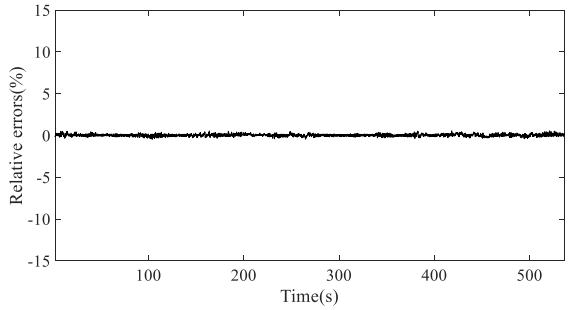

Figure 23. Relative errors between the estimated rotation speed using the AVBCF and the measured value.

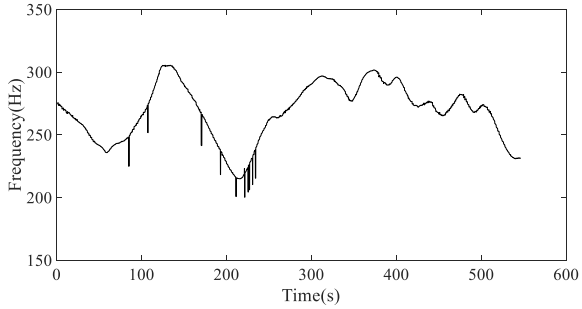

Figure 24. Extraction of the targeted ridge using the OSCF.

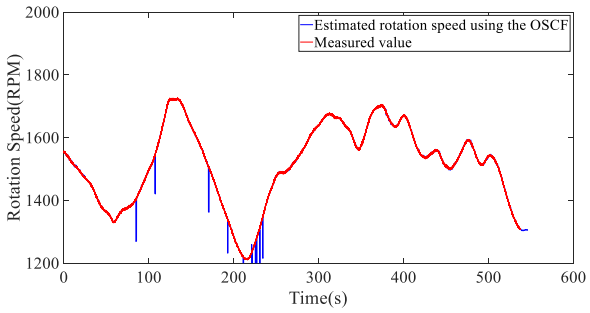

Figure 25. Comparisons between the estimated rotation speed using the OSCF and the measured value.

shows that some outliers in figure 17 have been removed from figure 18. Figure 19 describes the central line of the synthetic dispersive ridge and the confidence interval of the central line at 95% confidence level. Afterwards, the central line and the confidence interval were together projected to the targeted ridge in the ratio 10.3693 (kinematic relations between the second harmonic of the intermediate gear meshing frequency and the planet gear meshing frequency) according to table 2. The results projected are revealed in figure 20. As revealed in figure 20, the upper and lower boundaries of the confidence interval projected completely enclose the targeted ridge. Next, the AVBCF was exploited to extract the targeted ridge. Figure 21 manifests the extraction of the targeted ridge. In what follows, the rotation speed of the high speed shaft was deduced from the estimation of the targeted ridge according to the ratio $60 \times 119.95/(637.71 \times 2) = 5.6428$. Figure 22 draws a comparison between the estimated rotation speed using the AVBCF and the measured value. Figure 23 reveals relative errors between the estimated rotation speed using the AVBCF and the measured value. As indicated in figures 22

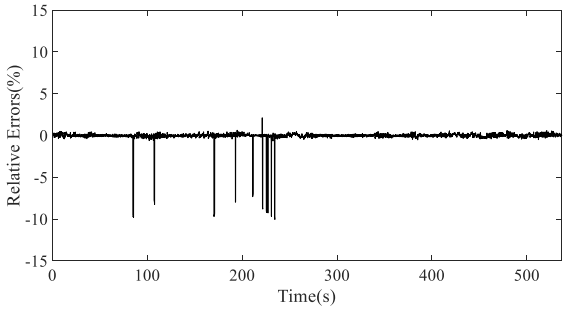

Figure 26. Relative errors between the estimated rotation speed using the OSCF and the measured value.

and 23, there are very minor differences between the estimated rotation speed using the AVBCF and the measured value. Also, to benchmark the performance of the AVBCF, the OSCF was used for the extraction of the targeted ridge and the results are depicted in figure 24. Figure 25 makes a comparison between the estimated rotation speed using the OSCF and the measured value. Figure 26 demonstrates relative errors between the estimated rotation speed using the OSCF and the measured value. As shown in figures 25 and 26, the estimated rotation speed using the OSCF deviates severely from the measured value at some instants when the rotation speed varies considerably. Thus, a comparison between figures 23 and 26 proves that the AVBCF delivers a better performance than the OSCF. Addtionally, there are very big differences between results provided by different contenders in CMMNO 2014 [19]. A comparison between figure 23 and the resutls provided in [19] points out that the AVBCF takes an advantage over those used in CMMNO 2014.

4.3. Discussion

This paper makes two main contributions. Firstly, dispersion of a ridge on a TFI of a signal is made profitable. In doing so, statistics of a dispersive ridge are estimated by analyzing edges of the dispersive ridge in a binary image. Furthermore, these statistics can indirectly provide a reference and searching regions for the targeted ridge. Secondly, the AVBCF is devised for ridge extraction. In this context, the central line of a synthetic dispersive ridge is projected to the targeted ridge for providing a real-time reference for the targeted ridge. Also, the confidence interval of the central line is projected to the targeted ridge for providing adaptive variable-bandwidth searching regions for the targeted ridge. As a consequence, the AVBCF seemingly overcomes the question occurring in the OSCF.

Although delivering a good performance in this paper, the AVBCF for ridge extraction still leaves some to be desired. To begin with, the resolution of a TFI is the key to maintaining the performance of the AVBCF. Higher resolution of a TFI will produce more accurate estimations of a targeted ridge. Accordingly, the AVBCF demonstrates a strong need for high resolution of a TFI. Secondly, an image zone with a relatively high SNR, providing a reference framework for a targeted ridge, is chosen manually. In the future, an intelligent

procedure should be developed for realizing automation of this choice. Thirdly, the AVBCF is sensitive to accuracy of a speed ratio. Thus, a speed ratio between a targeted ridge and a synthetic dispersive ridge must be calculated carefully for assuring accuracy of projections. Furthermore, the time-efficiency of the AVBCF is moderate and requires to be improved in the future.

5. Conclusions

Aiming at the shortage occurring in the OSCF, this paper puts forward the AVBCF for ridge extraction. In the AVBCF, a searching region of a point on a targeted ridge is independent of the previous neighbor of this point and has time-varying bandwidth. Afterwards, the performance of the AVBCF was benchmarked against the OSCF and some widespread methods. The results indicate that the AVBCF performs better than the other methods in ridge extraction. Thus, this paper seemingly paves a different way for use in ridge extraction. In the future, the AVBCF may be a promising method for ridge extraction of complex multicomponent signals.

Acknowledgments

The authors would like to kindly thank CMMNO 2014 for providing planetary gearbox vibration data. The work was supported by Shandong Provincial Natural Science Foundation (Project ZR2012EEL07) and Development Program of Science and Technology of Weifang City (Grant Nos. 2014ZJ1051, 2015GX023).

Appendix A. Canny edge detector

In an image, an edge is defined as a curve going along a path where image intensity changes sharply. Accordingly, an edge, which relates to a discontinuity of image intensity, indicates occurrences of important events or a change of natural properties [21]. Edge detection, used widely in image processing, machine vision and computer vision, aims to detect and describe discontinuities of intensity in an image [22]. By edge detection, a complex image can be outlined by edges. As a consequence, edge detection, which filters trivial information, can extract important structural features from an image. In this sense, edge detection is a powerful tool for simplifying analysis of an image.

Currently, many methods have been designed for edge detection, including the Sobel detector [23], the Prewitt detector [24], the Roberts detector [25], the Marr-Hildreth detector [26], the zero-cross detector [27] and the Canny detector [17]. Among these methods, the Canny detector is the most powerful [28]. A double threshold for detecting strong and weak edges is featured highly in the Canny detector. Additionally, the weak edges only connected to the strong edges will be preserved and the others abandoned [17]. Thus, the Canny detector is superior to the others in suppressing noise and preserving true weak edges [28].

The Canny detector is profiled in the following.

(1) Smooth the image $f(x,y)$ by a Gaussian filter for removing noise and unwanted details:

$$g(x,y) = G(x,y) * f(x,y) \tag{A.1}$$

$$G(x,y) = \frac{1}{2\pi\sigma^2}\exp\left(-\frac{x^2+y^2}{2\sigma}\right). \tag{A.2}$$

Here, $g(x,y)$ represents the smoothed image, $G(x,y)$ signifies a two-dimension Gaussian filter and the parameter σ indicates the standard deviation of Gaussian. Also, the sign '$*$' stands for convolution.

(2) Calculate magnitude and orientation of the intensity gradients of the smoothed image $g(x,y)$:

$$M(x,y) = \sqrt{g_x^2(x,y) + g_y^2(x,y)} \tag{A.3}$$

$$\theta(x,y) = \arctan\left[g_y(x,y)/g_x(x,y)\right] \tag{A.4}$$

$$g_x(x,y) = \frac{\partial g(x,y)}{\partial x}, \quad g_y(x,y) = \frac{\partial g(x,y)}{\partial y}. \tag{A.5}$$

Here, $M(x,y)$ and $\theta(x,y)$ mean the magnitude and the orientation of the intensity gradient, respectively.

(3) Suppress non-maximum gradient magnitude in $M(x,y)$ for thinning edges: if the current non-zero gradient value is larger than its two neighbors along the gradient direction $\theta(x,y)$, then the current value will remain unchanged. Otherwise, the current value is assigned to zero.

(4) Filter the thinned edges by two different thresholds T_1 and T_2 ($T_1 < T_2$) to acquire two different binary images I_1 and I_2.

(5) Remove all the weak edges that are not referable to the strong ones in the image I_2 from the image I_1 and connect the remaining edge segments in the images I_1 and I_2 for constructing the desirable edges.

Appendix B. Grubbs test

The Grubbs test, as a statistical test, serves to exclude outliers from a nearly normally distributed dataset [29]. For a dataset x_i, $i = 1, ..., N$, define the Grubbs statistic as $g_i = \frac{x_i - \bar{x}}{\sigma}$, where $\bar{x}$ and σ stand for the mean and the standard deviation of the dataset, respectively. After a significance level α is given, the Grubbs critical value $g_0(N,\alpha)$ is determined by solving the following probability equation:

$$P\{g_i \geqslant g_0(N,\alpha)\} = \alpha. \tag{B.1}$$

Afterwards, the Grubbs criterion is implemented: if $|x_i - \bar{x}| \geqslant \sigma g_0(N,\alpha)$, then exclude x_i from the dataset.

Appendix C. Confidence interval of a dispersive ridge

Construction of the confidence interval of a dispersive ridge is reported as follows. A dispersive ridge is outlined by its edges in a binary image filtered by the Canny detector. Suppose that x_j stands for edges of a dispersive ridge at the jth instant and x_j^k for the kth element of x_j, $k = 1, 2, ..., n$. Since the variance of x_j is unknown, the t-statistic should be adopted for estimating the confidence interval of the mean $\bar{x}_j = \sum_{k=1}^{n} x_j^k$, that is, $\frac{x_j - \bar{x}_j}{S_j/\sqrt{n}} \sim t(n-1)$. Here, $S_j^2 = \frac{1}{(n-1)} \sum_{k=1}^{n} \left(x_j^k - \bar{x}_j\right)^2$. Consequently, the confidence interval of the mean $\bar{x}_j$ at the confidence level $(1-\alpha)$ is estimated as $\left(\bar{x}_j \pm \frac{S_j}{\sqrt{n}} t_{\alpha/2}(1-n)\right)$. Typically, this paper sets $\alpha = 0.05$.

ORCID iDs

Jinshan Lin https://orcid.org/0000-0002-3163-9873

References

[1] Huang H, Baddour N and Liang M 2018 Bearing fault diagnosis under unknown time-varying rotational speed conditions via multiple time-frequency curve extraction *J. Sound Vib.* **414** 43–60

[2] Jiang X and Li S 2016 A dual path optimization ridge estimation method for condition monitoring of planetary gearbox under varying-speed operation *Measurement* **94** 630–44

[3] Delprat N, Escudie B, Guillemain P and Kronland-Martinet R 1992 Asymptotic wavelet and Gabor analysis: extraction of instantaneous frequencies *IEEE Trans. Inf. Theory* **38** 644–64

[4] Iatsenko D, Mcclintock P V E and Stefanovska A 2016 Extraction of instantaneous frequencies from ridges in time–frequency representations of signals *Signal Process* **125** 290–303

[5] Carmona R A, Hwang W L and Torrésani B 1999 Multiridge detection and time-frequency reconstruction *IEEE Trans. Signal Process.* **47** 480–92

[6] Tsai N-C, Li H-Y, Lin C-C, Chiang C-W and Wang P-L 2011 Identification of rod dynamics under influence of Active Magnetic Bearing *Mechatronics* **21** 1013–24

[7] Meignen S, Pham D-H and McLaughlin S 2017 On demodulation, ridge detection, and synchrosqueezing for multicomponent signals *IEEE Trans. Signal Process.* **65** 2093–103

[8] Chen S, Dong X, Xing G, Peng Z, Zhang W and Meng G 2017 Separation of overlapped non-stationary signals by ridge path regrouping and intrinsic chirp component decomposition *IEEE Sens. J.* **17** 5994–6005

[9] Wang Y, Peter W T, Tang B, Qin Y, Deng L, Huang T and Xu G 2019 Order spectrogram visualization for rolling bearing fault detection under speed variation conditions *Mech. Syst. Signal Process.* **122** 580–96

[10] He Q, Wang J, Hu F and Kong F 2013 Wayside acoustic diagnosis of defective train bearings based on signal resampling and information enhancement *J. Sound Vib.* **332** 5635–49

[11] Abid A, Gdeisat M, Burton D and Lalor M 2007 Ridge extraction algorithms for one-dimensional continuous wavelet transform: a comparison *J. Phys.: Conf. Ser.* **76** 012045

[12] Lin L and Ji H 2009 Signal feature extraction based on an improved EMD method *Measurement* **42** 796–803

[13] Zhu X, Zhang Z, Gao J and Li W 2019 Two robust approaches to multicomponent signal reconstruction from STFT ridges *Mech. Syst. Signal Process.* **115** 720–35

[14] Kowalski M, Meynard A and Wu H T 2018 Convex optimization approach to signals with fast varying instantaneous frequency *Appl. Comput. Harmon. Anal.* **44** 89–122

[15] Liu H, Cartwright A N and Basaran C 2004 Moiré interferogram phase extraction: a ridge detection algorithm for continuous wavelet transforms *Appl. Opt.* **43** 850–7

[16] Medina-Carnicer R, Muñoz-Salinas R, Yeguas-Bolivar E and Diaz-Mas L 2011 A novel method to look for the hysteresis thresholds for the Canny edge detector *Pattern Recogn.* **44** 1201–11

[17] Canny J 1986 A computational approach to edge detection *IEEE Trans. Pattern Anal.* **8** 679–98

[18] Randall R B, Coats M and Smith W A 2015 *Determining the Speed of a Variable Speed Wind Turbine from the Vibration Response* (Hunter Valley, CA: Acoustics)

[19] Leclère Q, André H and Antoni J 2016 PrésentationCMMNOcontestwopicts (www.researchgate.net/publication/299437545_PresentationCMMNOcontestwopicts)

[20] Leclère Q, André H and Antoni J 2016 A multi-order probabilistic approach for instantaneous angular speed tracking debriefing of the CMMNO14′ diagnosis contest *Mech. Syst. Signal Process.* **81** 375–86

[21] Barrow H G and Tenenbaum J M 1981 Interpreting line drawings as three-dimensional surfaces *Artif. Intell.* **17** 75–116

[22] Umbaugh S E 2016 *Digital Image Processing and Analysis: Human and Computer Vision Applications with CVIP Tools* (Boca Raton, FL: CRC Press)

[23] Sobel I and Feldman G 1968 A 3 × 3 isotropic gradient operator for image processing *A Talk at the Stanford Artificial Project* (Location: Palo Alto)

[24] Prewitt J 1970 Object enhancement and extraction *Picture Processing and Psychopictorics* eds B Lipkin and A Rosenfeld (New York: Academic) pp 75–149

[25] Roberts L G 1963 *Machine Perception of Three-Dimensional Soups* (Cambridge, MA: Massachusetts Institute of Technology)

[26] Marr D and Hildreth E 1980 Theory of edge detection *Proc. R. Soc.* B **207** 187–217

[27] Longuet-Higgins H 1987 A computer algorithm for reconstructing a scene from two projections *Readings in Computer Vision: Issues, Problems, Principles, and Paradigms* eds M A Fischler and O Fischler (San Franscisco, CA: Morgan Kaufmann) pp 61–2

[28] Shapiro L G and Stockman G C 2001 *Computer Vision* (London: Prentice Hall)

[29] Tomaya L C and Castro M D 2018 New estimation methods for the Grubbs model *Chemometr. Intell. Lab Syst.* **176** 119–25